ELSEVIER

Journal of Fluids and Structures 22 (2006) 77–98

JOURNAL OF FLUIDS AND STRUCTURES

www.elsevier.com/locate/jfs

Unsteady free-surface wave-induced boundary-layer separation for a surface-piercing NACA 0024 foil: Towing tank experiments

B. Metcalf, J. Longo, S. Ghosh, F. Stern*

IIHR—Hydroscience & Engineering, The University of Iowa, 100 C. Maxwell Stanley Hydraulics Laboratory, Iowa City, IA 52242-1585, USA

Received 17 December 2004; accepted 19 September 2005
Available online 27 October 2005

Abstract

Unsteady free-surface, wave-induced separation is documented using towing tank experiments for a surface-piercing NACA 0024 foil, which has insignificant separation, no wave effects, and 2-D flow in the deep. The test conditions are for minimal, reattaching, and nonreattaching separation: Froude numbers (Fr) = 0.19, 0.37, and 0.55 and Reynolds numbers = 0.822, 1.52, and 2.26×10^6. The measurements include mean far-field wave elevations for all three Fr, unsteady near-field wave elevations for medium and low Fr, mean foil-surface pressures for all three Fr, and unsteady foil-surface pressures for medium Fr. Unsteady measurements are statistically analyzed for mean, r.m.s., FFT, PSD, and phased-averaged organized oscillations and random fluctuation components. For Fr = 0.19, there is no separation and the expected Kelvin waves are present. For Fr = 0.37, the separation on the free and foil surfaces is demarcated by large r.m.s. (15–20% of the mean value dynamic range) and 1.94, 0.82, and 0.30 Hz dominant FFT frequency regions corresponding to shear layer, Karman shedding, and flapping instabilities, respectively. A large bow wave resembles a spilling breaker with low r.m.s. (2–5% of the mean value dynamic range) and 8.5 Hz dominant FFT frequency on the free and foil surfaces. Mean wave elevations in the separation region are relatively constant with intense free-surface oscillations, turbulence, and breaking. Outside the separation and wake region, the Kelvin waves are evident. The foil-surface pressure is high in the bow wave, low in the wave trough, gradually rises towards the trailing edge, and recovers 2-D distributions at large depths. For Fr = 0.55, the bow wave is enormous. The separation region moves towards the trailing edge with increased splashing and bubbles. The Kelvin waves are no longer distinguishable due to increased free-surface turbulence. The mean foil-surface pressure, free-surface, and bottom effects interact with each other. The combination of the present albeit relatively sparse experimental data with complementary computational fluid dynamics studies provides a credible description of the flow physics.

1. Introduction

Interactions between free-surface waves and surface-piercing body or structure boundary layers are of importance in the fields of ship, ocean, coastal, and hydraulic engineering. Wave-induced pressure gradients affect the boundary layer

*Corresponding author. Tel.: +1 319 335 5215; fax: +1 319 335 5238.
E-mail address: Frederick-stern@uiowa.edu (F. Stern).

0889-9746/$ - see front matter © 2005 Elsevier Ltd. All rights reserved.
doi:10.1016/j.jfluidstructs.2005.09.004

and vice versa, the boundary layer affects the waves having a first-order effect on forces and moments, damage and stability, and adverse local flow phenomena such as signatures. Under extreme conditions, waves induce or modify boundary-layer separation and the bodies or structures induce wave breaking both of which result in broken turbulent interfaces with air entrainment, vortices, and unsteady flow. Free surfaces also affect boundary-layer turbulence inducing vortices and wake spreading. The present interest is in unsteady free-surface, wave-induced, boundary-layer separation, i.e., separation solely induced by waves. The present topic is related to the general topic of unsteady 3-D boundary-layer separation (Kiya et al., 2000), geometrically similar topics of junction (Simpson, 2001), corner flow separations (Eisele et al., 2000), and specific topics of bluff surface-piercing or submerged body free-surface interactions (Sheridan et al., 1997; Oshkai and Rockwell, 1999; Li and Lin, 2001; Kawamura et al., 2002; Chen and Chwang, 2002; Lin and Li, 2003).

The physical problem is first identified by Chow (1967) using a surface-piercing foil designed for insignificant separation for the deep condition mounted on the floor of a hydraulic flume for a range of Froude numbers (Fr) and average Reynolds number $(\mathrm{Re}) = 7 \times 10^5$. Stern et al. (1989) make similar observations in their study of the effects of waves on the boundary layer of a surface-piercing flat plate with an upstream horizontal foil with variable depth of submergence used for generation of Stokes waves in a towing tank for a range of wave steepness Ak ($A2\pi/\lambda$) and average $\mathrm{Re} = 1.64 \times 10^6$. For medium Fr (foil) and large Ak (plate) separation is initiated just beyond the wave trough and extends to the foil trailing edge or following wave crest. On the free surface, the separation region is wedge shaped, broken, and turbulent. Vortex flow is evident towards the foil or plate and upstream with discontinuous wave elevations and capillary displacement waves near the upstream boundary. Beyond the separation starting point, the wave profile and elevations are fairly constant. The depth of separation is defined by reversed axial flow and upward cross flow, which is observed close to the foil surface in a wedge-shaped region gradually expanding from the separation starting point to a maximum depth near the foil trailing edge with a magnitude similar to the wave height.

Stern et al. (1993) perform laminar Navier–Stokes and turbulent Reynolds-averaged Navier–Stokes (RANS) steady-flow simulations with inviscid free-surface boundary conditions and a k–ε turbulence model with wall functions for a surface-piercing flat plate with an external Stokes wave, which simulates the Stern et al. (1989) experimental geometry. The separation starting point is over and under estimated for laminar and turbulent flow, respectively. The plate and free-surface streamlines display a saddle point of separation and a nodal point of attachment. Particle traces indicate an upward vortex towards the plate and upstream above the saddle point and a downstream vortex towards the plate and wake center plane beyond the saddle point. The separation region on the free surface and plate is qualitatively similar in shape and depth as described by Chow (1967) and Stern et al. (1989).

Zhang and Stern (1996) perform RANS steady-flow simulations with tracking free surface and Baldwin–Lomax turbulence modelling and wave-profile experiments for a surface-piercing NACA 0024 foil, which also has insignificant separation at large depths. The foil chord ($c = 1.2\,\mathrm{m}$) and draft ($T = 1.5\,\mathrm{m}$) are designed to achieve a large separation region and no-wave effects and 2-D flow at large depths to facilitate detailed flow field measurements. Test and simulation conditions are selected for minimal, reattaching, and nonreattaching separation: $\mathrm{Fr} = (0.2, 0.37, \text{and } 0.55)$ and $\mathrm{Re} = (0.822, 1.52, \text{and } 2.26 \times 10^6)$. Experimental wave profiles show similar results as Chow (1967) and Stern et al. (1989) with separation starting points $x = 0.41$, and 0.55 for the higher Fr. The separation is naturally unsteady with wave profile oscillations of about $\Delta z = 0.05$ and 0.1 for $\mathrm{Fr} = 0.37$ and 0.55, respectively. Simulations also show nearly constant wave profiles in the separation region, however, the separation starting points are over predicted $x = 0.95$, 0.22, and 0.46. For the higher Fr, separation extends to $x = 1.3$ into the wake. The usual Kelvin wave pattern is disrupted in the separation region, where the wave elevations are relatively flat with depressions near the vortex cores. The separation region on the free surface and plate is qualitatively similar in shape and depth as described by Chow (1967) and Stern et al. (1989). The nature of the flow in the separation region is qualitatively similar as Stern et al. (1993), but described in greater detail using a topological rule derived for free-surface, wave-induced separation in which free-surface streamlines are treated similarly as skin-friction lines. Additionally, a necklace vortex can be observed wrapping around the leading edge of the foil for higher Fr. Nodes and saddles of separation and attachment are identified and used to describe the flow patterns.

Pogozelski et al. (1997) also investigates free-surface, wave-induced separation for a surface-piercing strut in a towing tank for a range of Fr and average $\mathrm{Re} = 7.5 \times 10^5$. Breaking and splashing occur just beyond the wave trough (i.e., tow of the shoulder wave) at $x = 0.41$ for all $\mathrm{Fr} \geqslant 0.15$. For $\mathrm{Fr} = 0.255$ a downstream shoulder wave crest is evident, but for $\mathrm{Fr} = 0.36$ there is no distinct shoulder wave crest all the way to the trailing edge. The flow is increasingly more unsteady and violent for increasing Fr. For $\mathrm{Fr} \geqslant 0.255$, the shoulder wave and the separation region that forms behind it are dissipative such that the free surface is constant in the separation region with Kelvin waves only evident away from the model, but with a phase shift that starts in the bow wave trough. The authors point out that this phenomenon is similar to the results of Zhang and Stern (1996), but at different Fr which is attributed to

differences in body shape. For $Fr = 0.255$, the forward face of the bow wave resembles a spilling breaking wave, including capillary waves emanating from the toe, and underlying "necklace" vortex. In the separated region the total head is 50–60%, whereas for larger y the level is 70–80%. The wave breaking occurs only very close to the model (up to $y<0.2$). At $x = 0.64$, boundary-layer separation begins at the intersection of the model and the free surface. The separated region grows, but never extends far from the foil surface. The separation process originates from secondary flows associated with impingement and breaking at the root of the mid-body wave, which generates a series of pairs of longitudinal counter-rotating vortices. At $Fr = 0.255$, there is no reverse flow in the separation region, but at $Fr > 0.3$, flow reversal does occur. The authors point out that the necklace vortex and gross features of the separation region are similar to Zhang and Stern (1996), but structures within the separated region differ greatly and are attributed to the deficiencies of the RANS/Baldwin–Lomax model in accounting for wave breaking and the associated massive energy dissipation.

Also, of specific relevance are studies for surface-piercing circular cylinders, although in this case the deep flow exhibits unsteady 2-D separation. Kawamura et al. (2002) perform large-eddy simulations (LES) with tracking free-surface modelling for $Fr = 0.2$, 0.5, and 0.8 and $Re = 2.7 \times 10^4$, including comparisons with available experimental data. Results show fairly good agreement with data for mean and root-mean-square (r.m.s.) wave elevations and mean stream-wise velocity. The vortex shedding is attenuated within one diameter of the free surface at a high Fr, which is attributed to the inclination of the shear layers outward due to generation of surface waves. Studies of flow past a cylinder close to a free surface (Sheridan et al., 1997) show another shear layer can be generated from the free surface due to separation and appear adjacent to a layer from the cylinder surface to form a jet-like flow. Oshkai and Rockwell (1999) study the interaction of a horizontal cylinder with free-surface waves. They investigate the vorticity field below the free surface by changing the depth of the cylinder. The studies reveal that for low submergence of the cylinder, the vortex formation at the upper surface of the cylinder decreases whereas the lower surface vortex formation is enhanced. Another submerged body (foil) with free-surface, but 2-D, is studied by Chen and Chwang (2002), who find that the presence of a free-surface attenuates the Strouhal vortex frequency, yet delays the onset of a large-scale Karman instability and the occurrence of transitional behaviors. LES of wave interaction with a square cylinder is performed by Li and Lin (2001). They find that the inertial force normally dominates over the drag force by orders of magnitude for small Keulegan and Carpenter (KC) numbers. Their more recent studies (Lin and Li, 2003) focus on wave–current interaction with a vertical square cylinder, which demonstrates that the presence of waves can reduce both the strength and frequency of vortex shedding induced by a uniform current due to the nonlinear wave–current interaction. They also reveal the existence of three regions: initiating, growing, and decaying.

Previous studies have not yet fully explicated the nature of unsteady free-surface, wave-induced separation, which is the goal of the present complementary experimental and computational fluid dynamics (CFD) study. The geometry and conditions are the same as Zhang and Stern (1996). The present paper describes the experimental methods, conditions, uncertainty analysis, and results. The experiments include mean and unsteady wave elevations and foil-surface pressures and are admittedly sparse in comparison to the CFD results, but deemed sufficient for validation of the CFD and provide confidence for the combined results. Kandasamy et al. (2005) and Xing et al. (2005) provide the complementary unsteady RANS (URANS) and detached eddy simulation (DES) CFD solutions using both tracking and level-set free-surface modelling along with conditions, verification, validation, and diagnostics. The results include a review of and bringing to bear the most recent literature on unsteady 3-D separations and turbulence and detailed description of the unsteady separation vortices and turbulence. The overall results provide a credible description of the flow physics.

2. Experimental methods and conditions

2.1. Facility, coordinate system, and equipment

The experiments are conducted in an $h = 3.05$ m deep, $W = 3.05$ m wide, and $L = 100$ m long towing tank. The NACA 0024 foil is constructed of fiber-reinforced plexiglas and epoxy resin. Its principal dimensions include chord length $c = 1.2$ m, beam $B = 0.29$ m, and overall height $H = 2$ m, where the former is used to nondimensionalize the spatial coordinates for the presentation of the data. The foil coordinate system is defined with its origin at the intersection of the leading edge, calm-water plane, and center plane (Fig. 1, inset). The x-, y-, z-axes are directed downstream, transversely to starboard, and upward, respectively. An array of 182, 1-mm diameter pressure taps are installed on the starboard side covering the region $0.0613 \leqslant x \leqslant 0.8613$ and $-0.9304 \leqslant z \leqslant 0.1175$ which is based on the

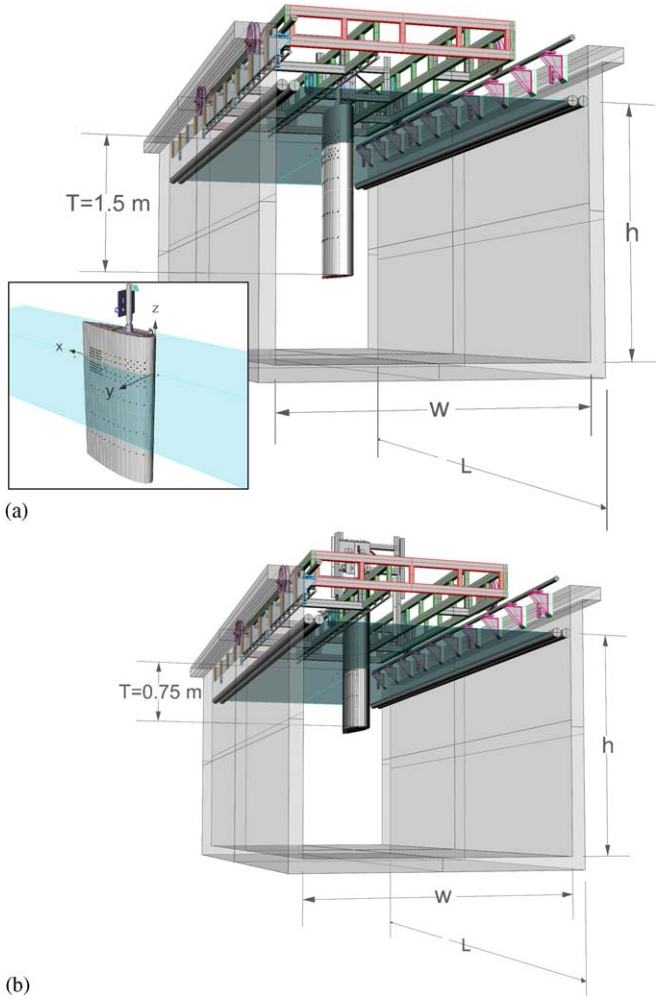

Fig. 1. Surface-piercing NACA 0024 foil model mounted in the towing tank ($h = 3.05$ m, $W = 3.05$ m, $L = 100$ m) showing deep and shallow drafts. The inset shows the NACA 0024 coordinate system and the entire surface pressure tap grid: (a) deep-draft condition and (b) shallow-draft condition.

RANS solutions of Zhang and Stern (1996). Nine pressure taps are installed on the port side for checking flow symmetry. Cylindrical studs of 4 mm height, 3.6 mm diameter, and 20 mm spacing, are fixed to the model at $x = 0.042$ for turbulence stimulation. Horizontal and vertical grid lines are scribed on the starboard side of the model. Model accuracy is checked using rulers and a plumb bob. The trailing edge is blunted starting at $x = 0.998$. Fig. 1 shows the surface-piercing NACA 0024 foil mounted to the model trailer at both deep $T = 1.5$ m and shallow $T = 0.75$ m drafts. Most data is for the deep-draft condition, but limited data for the shallow-draft condition is taken in order to assess restricted-water effects, as discussed later.

Mean far-field wave elevations are acquired for all three Fr using an array of three capacitance wires. The capacitance wires are mounted to a lightweight aluminum rack such that the wire spacing is $\Delta y = 36$ cm. The aluminum rack is affixed to a computer-controlled, 2-D traverse system which in turn is mounted to a horizontal, transversely oriented, wall-mounted beam over the tank and upstream of the drive carriage and model trailer. The traverses enable automated movement and positioning of the probes in the transverse (y) and vertical (z) coordinates. The probes are positioned and moved during the course of the experiments such that 36 equally spaced ($\Delta y = 0.025$) longitudinal cuts are acquired in a region $-2.0 \leqslant x \leqslant 3.0$ and $0.135 \leqslant y \leqslant 1.01$. A photoelectric switch pair affixed to the towing tank wall and model trailer initiates data acquisition when the leading edge of the foil is 14.955 m downstream of the capacitance wires. The

capacitance wires are statically calibrated using the automated vertical traverse. For each longitudinal cut, data is acquired at 100 Hz for 15 s. Data is reduced for mean values and contour plots. Unsteady near-field wave elevations are acquired for Fr = 0.19 and 0.37 using two, towed servo-mechanism wave probes (10 and 30 cm needles with 700 and 1200 mm/s response speeds, respectively). The probes are mounted to a 2-D automated traverse affixed to the model trailer and used to survey 976 locations covering the region $-0.5 \leqslant x \leqslant 1.48$, where $\Delta y \leqslant 0.135$ for $x < -0.0325$, $\Delta y \leqslant 0.27$ 4 for $x < 0.375$, and $\Delta y \leqslant 0.459$ for $x \geqslant 0.38$ (where Δy is measured from the center-plane or foil surface). The servo-mechanism wave probes are also statically calibrated using the automated vertical traverse. For each measurement location, data is acquired at 410 Hz for 10 s which limits the maximum resolvable frequency to 205 Hz. The full-scale, amplitude–frequency response for the 10- and 30-cm wave probes is 2.2 and 0.7 Hz, respectively, but up to 100 Hz for amplitudes up to 1 mm. In consideration of the servo wave gage amplitude–frequency performance envelope and the measured r.m.s. values in the near-field, it is felt that the wave probes are capable of resolving the full range of the free-surface frequencies in the present study. Fig. 2 shows the far- and near-field measurement grids and analysis and precision limit locations. Metcalf (2001) compares and shows that the far- and near-field wave elevation data overlap within the estimated uncertainties.

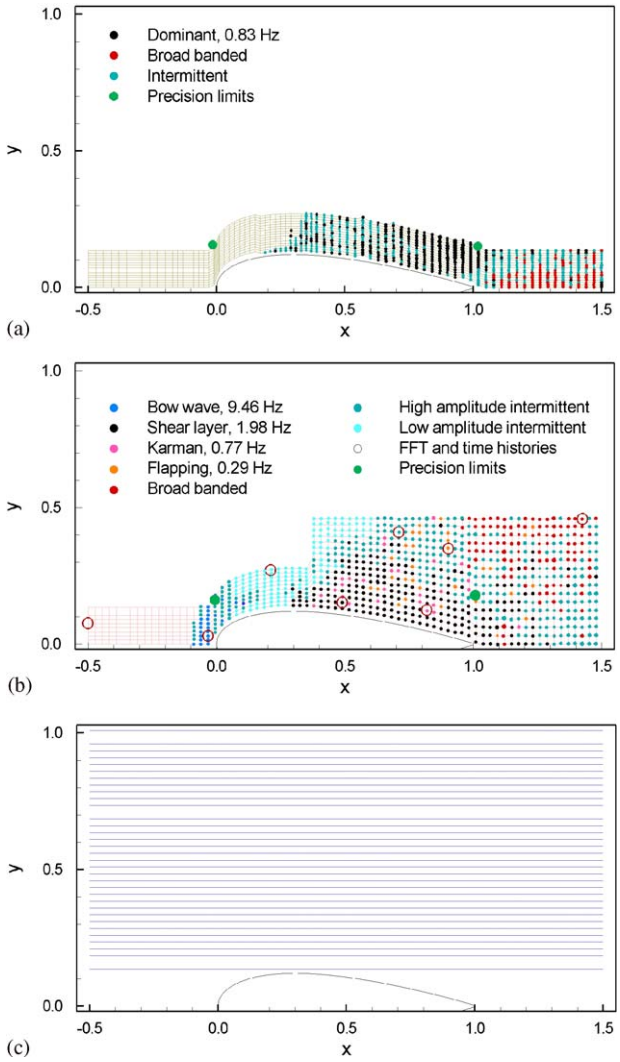

Fig. 2. Near- and far-field wave elevation grids showing analysis and precision limit measurement locations: (a) Fr = 0.19 near-field wave elevation grid; (b) Fr = 0.37 near-field wave elevation grid and (c) Fr = 0.19, 0.37, 0.55 far-field wave elevation grid.

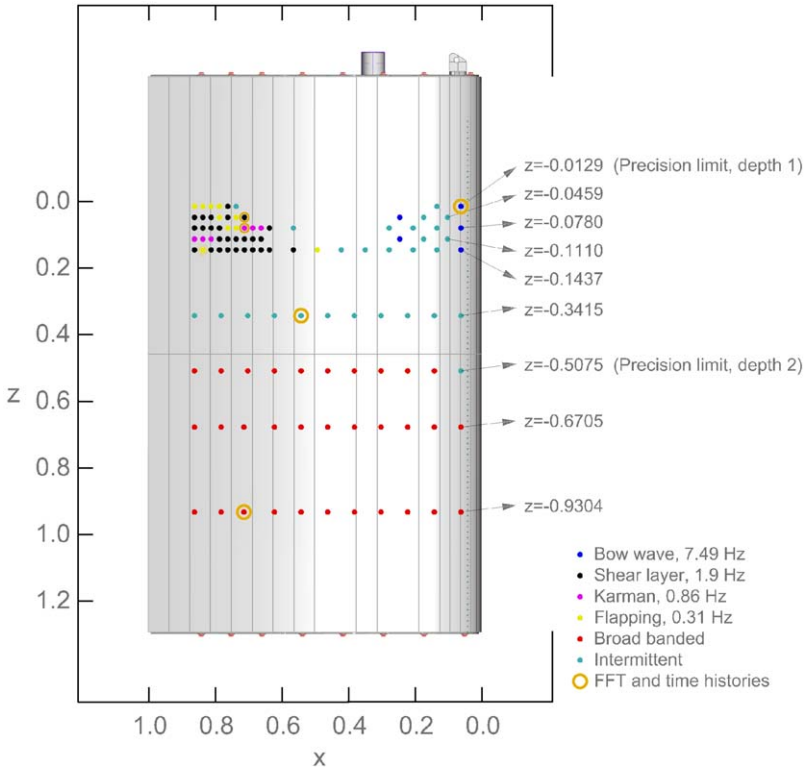

Fig. 3. Surface pressure tap grid showing analysis and precision limit measurement locations for Fr = 0.37.

Surface pressures are measured using an upstream $(x, y, z) = (-2.0, 0.0, -0.04)$ Pitot-static tube and ten Validyne DP 15 variable-reluctance, differential pressure transducers and signal conditioners. The transducers are fitted with 2.21 kPa pressure-sensitive diaphragms. Each transducer-signal conditioner pair are capable of DC output from steady state to 1 kHz. The negative pressure ports are plumbed into a manifold, which in turn is plumbed to the static-pressure holes on the Pitot-static probe for sensing the upstream, uniform-flow reference pressure. The positive pressure ports are coupled to ten different surface-pressure taps on the NACA 0024. The overall system maximum frequency response is estimated to be 40 Hz (0.025 s period) due to the tubing response limitations. The differential pressure transducers are statically calibrated using an automated vertical traverse with stationary and movable water baths. For each pressure tap, data is acquired at 91 Hz for 11 s for Fr = 0.19 and 0.55 and 91 Hz for 16 s for Fr = 0.37. For low and high Fr only, mean data is acquired using a 1 Hz low-pass filter, whereas for medium Fr additionally unsteady data is acquired using a 1 kHz filter. Fig. 3 shows the surface-pressure measurement grid and analysis and precision limit locations.

The drive carriage and model trailer are accelerated to steady speed over the first 20% of the towing tank using a ramp function designed to minimize transient effects, which leaves about 70% of the towing tank distance for data acquisition and the final 10% for stopping. Movable sidewall wave dampeners and a fixed beach at the downstream end enable 10 min intervals between the carriage runs. Steady data is reduced to mean values and unsteady data is additionally statistically analyzed for r.m.s., fast-Fourier transform (FFT), and power-spectral density (PSD) values. Unsteady data in regions with dominant FFT frequency are further analyzed for organized oscillation and random fluctuation components using a zero-phase averaging technique (Sung and Yoo, 2001). The phase-averaging technique includes a 5-point average filter, identification of peaks using zero gradients and sign changes, zero phase averaging using local nondimensional period, and reconstructed organized oscillation and random fluctuation based on their difference with the raw measured value. The technique performs optimally for time histories with narrowly banded dominant FFT frequency.

Table 1
Uncertainties for far-field free-surface elevations $U_{\zeta FF}$

Term	Fr = 0.19		Fr = 0.37		Fr = 0.55	
	Magnitude	%	Magnitude	%	Magnitude	%
$B_x\theta_x$	−7.9994e−06	0.01[a]	−3.7627e−05	0.15[a]	2.0632e−05	0.01[a]
$B_y\theta_y$	3.4395e−06	0.0[a]	5.6832e−06	0.0[a]	3.0105e−06	0.0[a]
$B_z\theta_z$	7.2196e−04	99.99[a]	9.668 1e−04	99.85[a]	3.5108e−03	99.99[a]
$B_{\zeta FF}(x,y)$	7.22e−04	*58.5*	9.68e−04	*8.94*	3.51e−03	*24.39*
$P_{\zeta FF}(x,y)$	6.08e−04	*41.5*	3.13e−03	*91.06*	6.20e−03	*75.61*
$U_{\zeta FF}(x,y)$	9.44e−04	**2.25**	3.28e−03	**2.48**	7.13e−03	**4.22**
$DR_{\zeta NF/\zeta FF}$	0.0418		0.132		0.169	
Max	$\zeta_{NF/FF} = 0.0172$ ($x = -0.01$, $y = 0.009$)		$\zeta_{NF/FF} = 0.0559$ ($x = -0.0325$, $y = 0.0$)		$\zeta_{NF/FF} = 0.09$ ($x = -0.09$, $y = 0.135$)	
Min	$\zeta_{NF/FF} = -0.0246$ ($x = 0.17$, $y = 0.126$)		$\zeta_{NF/FF} = -0.0761$ ($x = 0.352$, $y = 0.171$)		$\zeta_{NF/FF} = -0.16$ ($x = 0.603$, $y = 0.185$)	

Note: a is % of B_r^2 range; italic is % of U_r^2 range; bold is % of dynamic range (DR) of result.

Table 2
Uncertainties for near-field free-surface elevations $U_{\zeta NF}$

Term	Fr = 0.19		Fr = 0.37			
	Magnitude	%	Bow		Wake	
			Magnitude	%	Magnitude	%
$B_x\theta_x$	−2.9336e−06	0.0[a]	5.6400e−05	1.7[a]	5.6400e−05	1.7[a]
$B_y\theta_y$	5.4361e−06	0.2[a]	4.4634e−06	0.2[a]	4.4634e−06	0.2[a]
$B_z\theta_z$	2.1900e−04	99.8[a]	3.0100e−04	98.1[a]	3.0100e−04	98.1[a]
$B_{\zeta NF}(x,y)$	2.1909e−04	*85.46*	3.0627e−04	*18.56*	3.0627e−04	*4.17*
$P_{\zeta NF}(x,y)$	8.9700e−05	*14.54*	6.4159e−04	*81.44*	1.4e−03	*95.83*
$U_{\zeta NF}(x,y)$	2.37e−04	**0.57**	7.1094e−04	**0.54**	1.5e−03	**1.14**
$DR_{\zeta NF/\zeta FF}$	0.0418		0.132		0.132	
$B_{r.m.s.NF}(x,y)$			3.0627e−04	*89.21*	3.0627e−04	*14.11*
$P_{r.m.s.NF}(x,y)$			1.0654e−04	*10.79*	7.407e−04	*85.89*
$U_{r.m.s.NF}(x,y)$			3.2427e−04	**1.65**	8.154e−04	**4.16**
$DR_{r.m.s.NF}$			0.0196		0.0196	
			Max r.m.s. = 0.0199 ($x = 0.38$, $y = 0.139$)			
			Min r.m.s. = 0.0003 ($x = -0.473$, $y = 0.045$)			

Note: a is % of B_r^2 range; italic is % of U_r^2 range; bold is % of dynamic range (DR) of result.

Table 3
Uncertainties for surface pressures U_{Cp}

Term	Fr = 0.19		Fr = 0.37		Fr = 0.55	
	Magnitude	%	Magnitude	%	Magnitude	%
$B_x\theta_x$	1.5000e−05	0.00[a]	1.5000e−05	0.00[a]	1.5000e−05	0.00[a]
$B_z\theta_z$	1.7000e−05	0.00[a]	1.7000e−05	0.00[a]	1.7000e−05	0.00[a]
$B_{Cp}\theta_{Cp}$	2.4700e−02	100.00[a]	7.7100e−03	100.00[a]	6.8000e−03	100.00[a]
$B_{Cp}(x,y)$	2.475e−02	*95.7*	7.71e−03	*12.75*	6.80e−03	*53.75*
$P_{Cp}(x,y)$	3.57e−03	*4.3*	2.785e−02	*87.25*	6.31e−03	*46.25*
$U_{Cp}(x,y)$	2.53e−02	**1.55**	2.98e−02	**2.52**	9.48e−03	**0.57**
DR_{Cp}	1.632		1.183		1.672	
Max	$C_p = 0.0418$ ($x = -0.861$, $z = -0.0459$)		$C_p = -0.017$ ($x = -0.861$, $z = -0.93$)		$C_p = 0.841$ ($x = 0.0613$, $z = -0.118$)	
Min	$C_p = -1.59$ ($x = 0.191$, $z = -0.0129$)		$C_p = -1.2$ ($x = -0.361$, $z = -0.1437$)		$C_p = -0.831$ ($x = 0.521$, $z = -0.1437$)	

Note: a is % of B_r^2 range; italic is % of U_r^2 range; bold is % of dynamic range (DR) of result.

2.2. Uncertainty analysis

Uncertainty analysis procedures follow international standards (ASME, 1998; ITTC, 2002). Tables 1–3 provide bias and precision limits and total uncertainties for far- and near-field wave elevations and surface pressure measurements, respectively. The model has a slight twist such that the leading edge is plumb along its full height, but the bottom trailing edge is displaced 2.3 mm towards the port side. The model offsets are otherwise estimated within 0.2% of c. For wave profiles at each Fr the average $U_\zeta = 2.0\%$ of the wave profile dynamic range (DR_ζ). Bias limits include positional accuracies of the measurement station lines on the model, and precision limits are based on three repeat tests for each Fr. Far-field wave elevations at each Fr average $U_{\zeta\mathrm{FF}} = 3.0\%$ of $DR_{\zeta\mathrm{FF}}$. Bias limits include positioning and calibration of the capacitance wire probes, and precision limits are based on four and six repeated tests for low and medium/high Fr, respectively. Near-field wave elevations at each Fr average $U_{\zeta\mathrm{NF}} = 0.75\%$ of $DR_{\zeta\mathrm{NF}}$. Bias limits include positioning and calibration of the servo mechanism wave probes, and precision limits are based on 11 repeated tests at two locations $(x, y) = (0.0, 0.135)$ and (1.0, 0.135) for both Fr. For $\mathrm{Fr} = 0.37$, the total uncertainty of the wave elevation is $U_{\zeta\mathrm{NF}} = 0.54\%$ of $DR_{\zeta\mathrm{NF}}$ at the bow and $U_{\zeta\mathrm{NF}} = 1.14\%$ of $DR_{\zeta\mathrm{NF}}$ at the wake. The total uncertainty of the r.m.s. of the near-field elevation is $U_{\mathrm{r.m.s.NF}} = 1.65\%$ of $DR_{\mathrm{r.m.s.NF}}$ at the bow and $U_{\mathrm{r.m.s.NF}} = 4.16\%$ of $DR_{\mathrm{r.m.s.NF}}$ at the wake for medium Fr. For surface pressure at each Fr, the average $U_{Cp} = 1.55\%$ of DR_{Cp}. The bias limits include location of the surface pressure taps, calibration of the pressure transducers, and carriage speed. Precision limits are based on ten repeated tests at two depths $z = (-0.0129, -0.5075)$ and all three Fr. Uncertainty intervals for all measurements are reasonable in comparison with other geometries for the same and different towing tank facilities (Stern et al., 2005; Longo and Stern, 2005).

2.3. Restricted-water and foil-bottom effects

Table 4 compares ITTC (2002) recommendations for avoiding restricted-water effects with values for the present and related studies model geometries. For Fr_h exceeding 0.7 the wave resistance is affected. If the water-depth/model-draft ratio is <4 there exists an influence on the flow surrounding the model, independent of Fr_h. If $W/c < 0.35$, there is an influence of bow wave reflection from the lateral boundary on the stern flow, and $W/B < 4$ signifies that the flow surrounding the model is affected. The present model satisfies all but the water-depth/model-draft ratio, which is intentionally violated to permit recovery of the deep, no-wave, and 2-D condition. Other studies violate this and the waterway-section/mid-body section area ratio condition.

Limited far-field wave elevations ($y = 0.135$, 0.435, 0.735, and 1.01) and surface-pressure measurements at $z = -0.28$ are also made for a shallow-draft condition and $\mathrm{Fr} = 0.37$, which does not violate the water-depth/model-draft ratio condition, to assess restricted-water and foil-bottom effects. For shallow draft, the wave and wake envelope is widened, which shifts the crests and troughs slightly upstream, and the wave elevation in the separation region is slightly larger. The differences are systematic, but are of the same order as the uncertainty in the measurements. For deep draft and $-0.3 \leqslant z \leqslant -0.72$, the surface pressure is nearly 2-D (small span-wise gradient), however, there is increased and decreased pressures on the fore and after chord, respectively, in comparison to 2-D inviscid theory. Fore-chord differences are attributed to viscous effects since they have the same magnitude as for the $\mathrm{Fr} = 0.19$ case and are in agreement with 2-D RANS solutions. After-chord differences are attributed to a combination of free-surface and bottom effects. For $z > -0.3$, free-surface effects are evident such that the average reduction of pressure from the 2-D distribution ($z = -0.60$) is 22% of DR_{Cp} and the distribution follows the wave profile. For $z < -0.72$, bottom effects are

Table 4
Restricted-water effects for experimental studies

Criteria	Chow	Zhang and Stern	Pogozelski et al.	Deep-draft	Shallow-draft
$\mathrm{Fr}_h = \frac{U_c}{\sqrt{gh}} \leqslant 0.7$	0.13–0.31	0.12–0.35	0.04–0.4	0.12–0.35	0.12–0.35
$\frac{h}{T} \geqslant 4$	1	2	1.1	2	4
$\frac{W}{c} \geqslant 0.35$	2.33	2.5	3.33	2.5	2.5
$\frac{W}{B} \geqslant 4$	8.97	10	10	10	10
$\frac{A_t}{A_M} = \frac{Wh}{BT} \geqslant 15$	7.58	20.8	11.1	20.8	41.7

evident such that the distribution is similar to the 2-D case, but with an average increase of 8% of DR_{Cp}. For shallow draft and $z = -0.28$, the distribution shape is similar to the deep-draft case at the same depth, but with an average increase of 13% of DR_{Cp}. A 9% of DR_{Cp} increase is attributed to bottom effects since the location of the C_p measurement is also $\Delta z = 0.027$ from the bottom of the foil such that only a 4% of DR_{Cp} increase can be attributed to blockage.

Kandasamy (2001) investigates restricted-water and foil-bottom effects through steady RANS solutions for infinite draft ($z_{\min} = -1.0$ and -2.0 with symmetry bottom condition), deep draft ($h/T = 2.0$ with slip foil bottom condition), and shallow draft ($h/T = 3.0$ with slip foil bottom condition) conditions without towing-tank walls and deep draft (with no-slip foil bottom condition) with towing-tank walls for Fr = 0.37. Results in the 2-D region indicate a 5% of DR_{Cp} average increase in pressure for deep draft with walls. Half of the increase is due to the finite draft and the other half is due to the walls. The results in the free-surface region are relatively insensitive to draft and the presence of the walls. The bottom effects are similar to the EFD in showing increases in pressure over the lower-third of the foil. A teardropped-shaped separation bubble is also predicted on the foil bottom near the leading edge (25% of c in length and 10% of c in height).

3. Results

Photographs of the surface-piercing NACA 0024 foil for all three Fr are shown in Fig. 4. For Fr = 0.19, there is no separation and the Kelvin wave system dominates, but with relatively large bow wave and wide wake due to the blunt bow and large beam and draft compared to a usual ship. Some free-surface roughness and turbulence is observed in a trapezoid-shaped region near the after-body and wake. For Fr = 0.37, the bow wave increases dramatically, breaks, and wraps around the bow with features similar to spilling breakers, including capillary waves in front of the toe. Wave-induced separation initiates just beyond the shoulder-wave trough ($x \approx 0.34$). A wedge-shaped region with relatively constant mean wave elevations and intense free-surface oscillations, turbulence, and breaking is observed. Splashing and bubbles are most intense in the toe and the sharp front of the separation region with the center near $(x, y) = (0.5, 0.363)$ about which the free-surface flow rotates in a clockwise direction on the starboard side. The wake region is also wide with relatively constant mean wave elevations and free-surface oscillations and turbulence. Outside the separation and wake region the usual Kelvin waves are evident. For Fr = 0.55, the bow wave is enormous and nearly spans the towing tank width. The region of boundary-layer separation is reduced and shifted towards the trailing edge ($x \approx 0.525$), wedge shaped, and spans the towing tank with increased splashing and bubbles. The Kelvin waves are less distinguishable due to very-large, free-surface oscillations and turbulence with the appearance of a hydraulic jump.

Fig. 5 shows mean wave elevation contours for all three Fr, which display details of the previously described photographs. Contour levels for medium and high Fr are 5 and 7.5 times greater than those for low Fr, respectively. The wave envelope of the diverging and transverse waves is smaller (15 deg) for low Fr and larger (35–40 deg) for medium and high Fr than the 19° Kelvin wave value. The diverging waves are more prominent than the transverse waves with wave lengths comparable to the Kelvin wave values, where the transverse wave length is defined as $\lambda_t = 2\pi \mathrm{Fr}^2$ and the diverging wave length is defined as $\lambda_d = \lambda_t/1.49$.

Fig. 6(a)–(c) shows contours of wave elevation r.m.s. for medium Fr. Maximum r.m.s. values are about 15% of DR_ζ, which is much greater than the measurement uncertainty. The largest magnitudes are for a semi-elliptical region near the shoulder and after-body with major axis beginning and ending on the foil surface at $x = 0.3$ and 1.0, respectively, and semi-minor axis beginning and ending on the foil surface and outer measurement boundary at $y = 0.48$, respectively. In addition, r.m.s. magnitudes (about 2% of DR_ζ) are relatively smaller for regions around the bow, upstream of the separation region, and in the wake. Table 5 summarizes average and maximum r.m.s. values for bow and separation regions.

Fig. 6(d) and (e) shows the dominant FFT frequency of the wave-elevation contours. Near the bow region, the average dominant FFT frequency is 9.46 Hz, and in the separation region it is mostly 1.98 Hz both of which are obvious features of the EFD data without recourse to the CFD. URANS and DES both show three distinct regions in the separation region: (i) the high-frequency 2 Hz region within the separation region (shear layer instability dominates); (ii) the intermediate-frequency 0.74 Hz region immediately following reattachment (Karman-type instability dominates); and (iii) the low-frequency 0.32 Hz region around the Kelvin wave crest (flapping instability dominates). All three are also evident in the EFD, but not quite as distinct.

Wave elevation time histories with running mean and r.m.s., FFT, and PSD are closely examined at all near-field data locations for both low and medium Fr to identify regions with steady and unsteady response and for the latter dominant, intermittent, or broad-banded FFT frequencies. For low Fr, the maximum r.m.s. values are about 3.3% of

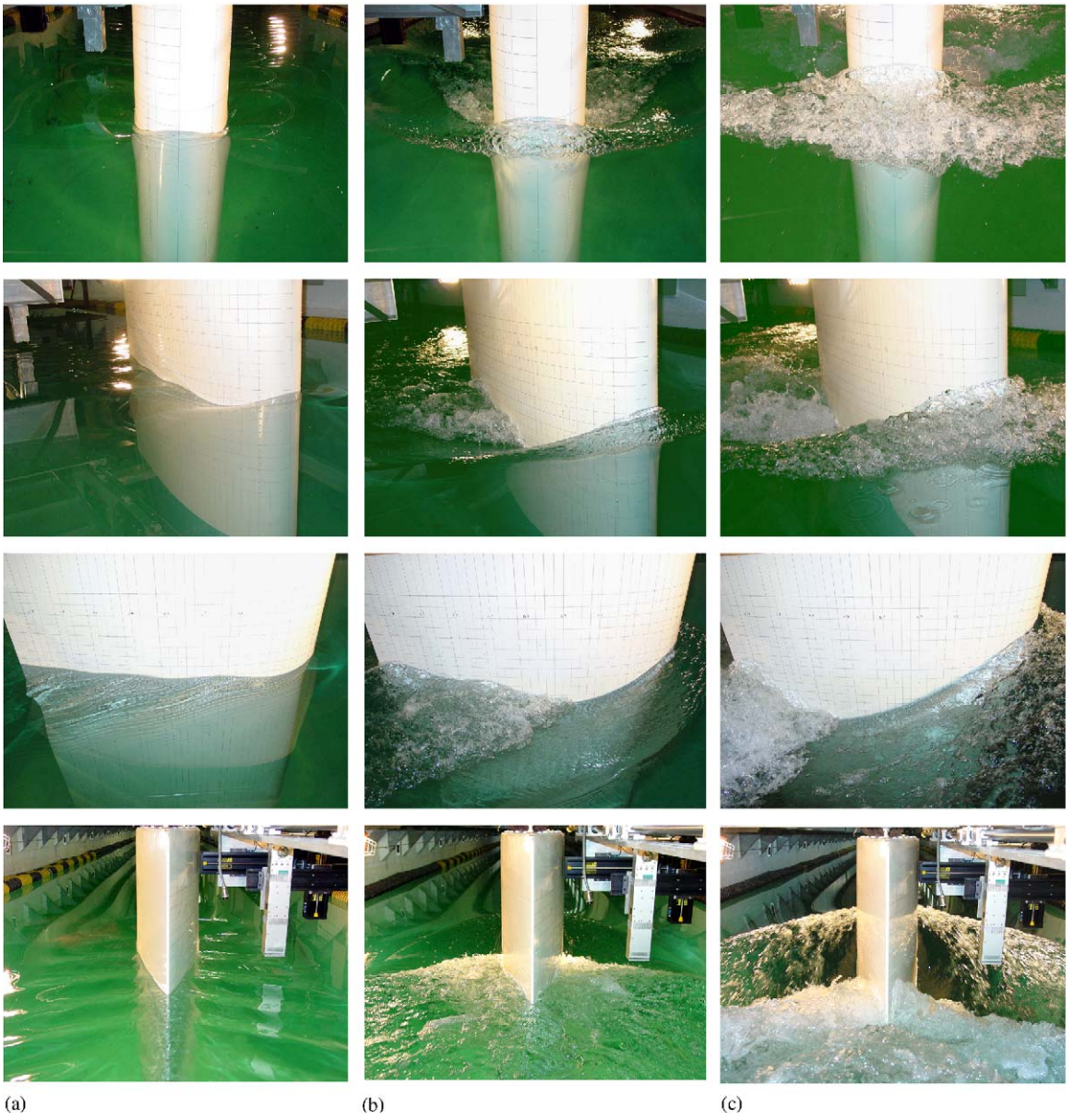

Fig. 4. Photographs of the NACA 0024 wave field for three Fr: (1) row 1, bow region; (2) row 2, front-quarter view; (3) row 3, side view of wave profile; (4) row 4, wake region: (a) Fr = 0.19; (b) Fr = 0.37 and (c) Fr = 0.55.

$DR_{\zeta NF}$, which is of similar magnitude to the estimated measurement uncertainty based on Fr = 0.37 estimates and the reason the r.m.s. is not presented here. However, in the aforementioned trapezoidal region where free-surface roughening and turbulence are observed, many locations display unsteady responses as labelled in Fig. 2(a). For medium Fr, unsteady responses show an average high dominant FFT frequency of 9.46 Hz in a small region of low r.m.s. near the bow and a region of average shear layer (SL, 1.98 Hz), Karman (0.77 Hz), and flapping (0.29 Hz) dominant FFT frequencies in the large region of high r.m.s. Both cases are bounded by regions of intermittent response. In the outer wake, the response is broad banded. Responses labelled in Fig. 2(b) with time histories, expanded views of time histories, and FFT and PSD at representative locations are shown in Fig. 7 where the abscissa for the FFT and PSD is nondimensional frequency or Strouhal number and defined as $St = fc/U_c$. Fig 7(a) shows the steady-flow

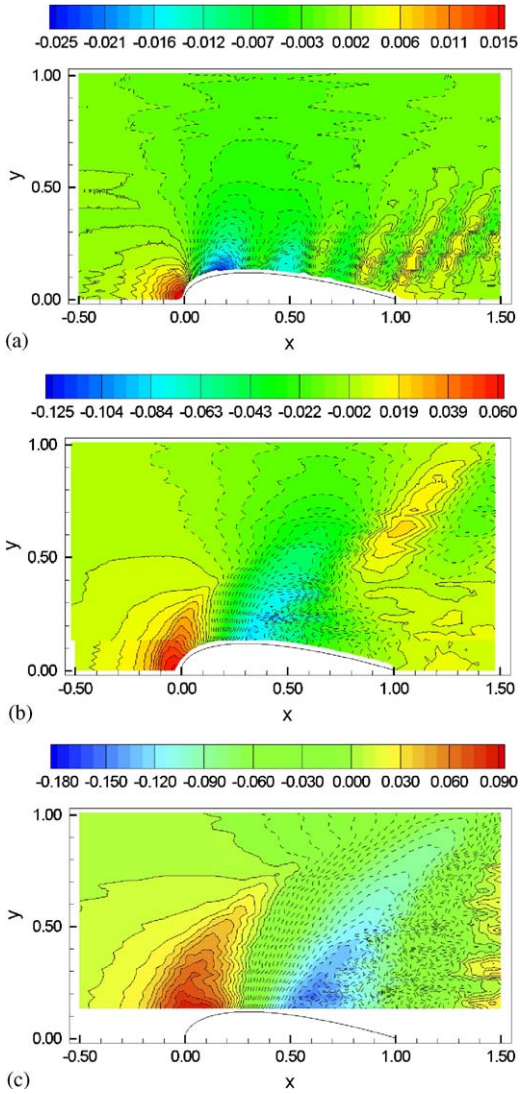

Fig. 5. Free-surface elevation—mean: (a) Fr = 0.19; (b) Fr = 0.37 and (c) Fr = 0.55.

response. Fig. 7(b) shows the high, dominant FFT frequency response with low r.m.s. oscillations evident, especially in the expanded view and FFT. Fig. 7(c) shows the low-amplitude intermittent frequency response. Fig. 7(d) shows the SL dominant FFT frequency response with high r.m.s. oscillations evident, especially in the expanded view and FFT. High and SL dominant FFT frequency responses clearly display effects of both organized oscillations and random fluctuations such that the r.m.s. includes both. Organized component average values are 1.4% and 14.4% of $DR_{\zeta NF}$ for the bow and separation regions, respectively. Random component average values are 1.3% and 7.0% of $DR_{\zeta NF}$ for the two regions as also shown in Figs. 6(b), (c), (f), (g) and 7(b), (d) and summarized in Table 5. Organized oscillations display narrow-banded FFT, whereas random fluctuations display broad-banded FFT. Visually as seen in photographs, the unsteady responses seem to be dominated by random fluctuations masking organized oscillations near the bow and toe of the separation region. Fig. 7(e)–(g) show Karman, flapping, and high-amplitude intermittent FFT frequency responses, respectively. Fig. 7(h) shows a broad-banded response. For all unsteady responses, the PSD show high- and very-high-frequency decay with slopes of about −2 and −3, respectively, which has been observed for the dissipation of turbulence near a free surface and attributed to onset of 2-D turbulence near a free surface (Orlins and Gulliver, 2000).

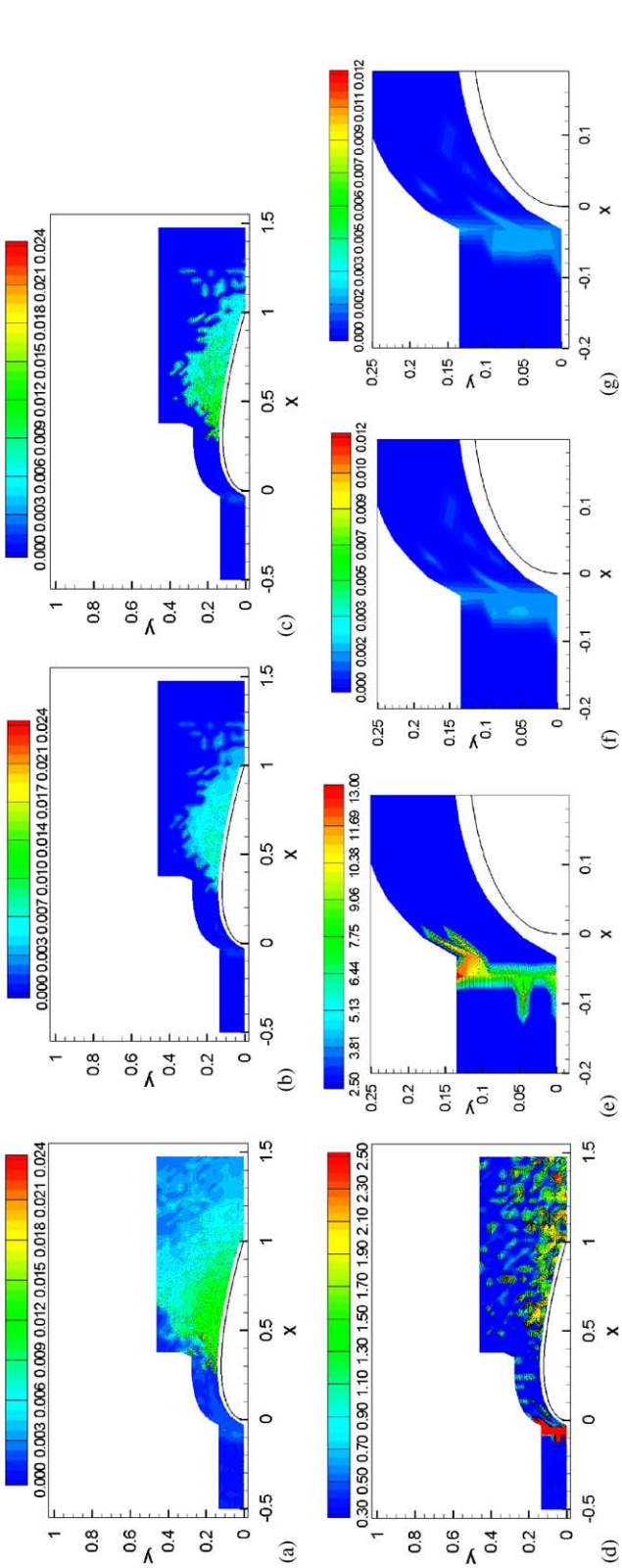

Fig. 6. Free-surface elevation—r.m.s. and dominant frequency for Fr = 0.37: (a) r.m.s. of raw wave elevation; (b) r.m.s. of organized oscillation; (c) r.m.s. of random fluctuation; (d) dominant FFT frequency; (e) expanded view of dominant FFT frequency region; (f) expanded view of organized oscillation (bow region) and (g) expanded view of random fluctuation (bow region).

Table 5
R.m.s. of near-field free surface for Fr = 0.37

	Wave elevation (Dynamic range, $DR_{\zeta NF} = 0.132$)					
	Bow region			Separation region		
	Raw	Organized	Random	Raw	Organized	Random
r.m.s. (average)	0.001793	0.00153	0.00115	0.00653	0.00716	0.000479
r.m.s. (max)	0.0026	0.001843	0.00174	0.0199	0.01895	0.00928
r.m.s. (max)/$DR_{\zeta NF}$	1.96%	1.39%	1.32%	15.07%	14.35%	7.03%

Fig. 8 compares Zhang and Stern (1996) wave profile measurements with the present near-field wave elevations along the center-plane upstream and down stream of the foil and $\Delta y = 0.025$ off the foil surface for low and medium Fr. For low Fr, wave profile and mean wave elevation data is in close agreement. For medium Fr, wave profiles and mean wave elevations for the bow wave are in close agreement. Whereas wave elevations show separation starting at a point $x = 0.275$, with a more gradual rise towards the trailing edge, and smaller oscillations than the wave profiles, which show separation starting at a point $x = 0.4$, with a steeper rise and larger oscillations. For high Fr, the wave profile separation starting point is delayed until $x = 0.525$ and oscillations are larger than for the medium Fr. Also shown in Fig. 8 is data from Zhang and Stern (1996) for lower Re taken using a smaller $c = 0.15$ m NACA 0024 model, which shows increased regions of separation with separation starting points at $x = 0.2$ and 0.475 for medium and high Fr, respectively. Maximum and minimum elevations are on the foil surface at the bow and first wave trough with values of (0.025, 0.075, 0.125) and (−0.04, −0.1, −0.15), respectively, for low, medium, and high Fr, respectively.

Fig. 9 shows the mean foil-surface pressure contours for all three Fr. For low and medium Fr, free-surface effects penetrate to $z = -0.15$ and −0.3 and bottom effects are evident for $z < -0.8$ and −0.72, respectively, whereas for intermediate depths, the pressure distribution is nearly 2-D, as previously discussed with regard to restricted-water effects. For high Fr, free-surface and bottom effects interact with each other and it is not possible to identify the 2-D, pressure distribution region. For low Fr, typical wave effects are displayed, including the bow and subsequent wave crest and trough, high- and low-pressure regions with about one wavelength penetration depth, and gradual stern wave pressure rise towards the trailing edge. For higher Fr, the bow wave crest (high pressure) and trough (low pressure) with about one wave height penetration depth is followed by a gradual constant depth-wise pressure rise towards the trailing edge.

Fig. 10(a)–(c) shows contours of foil-surface pressure r.m.s. for medium Fr. Maximum r.m.s. values are about 20% of DR_{Cp}. The largest r.m.s. magnitudes are for an elliptical-shaped region initiating just beyond the wave trough and extending to the trailing edge with a penetration depth similar to the wave height. In addition, a relatively smaller r.m.s. magnitude (about 5% of DR_{Cp}) region is below the bow wave. Peak values are seen along a track between $x = 0.6$ and the trailing edge at a depth of $z = -0.125$. Table 6 summarizes average and maximum r.m.s. values for the bow and separation regions.

Fig 10(d, e) shows contours of foil-surface pressure dominant FFT frequency for medium Fr. Near the bow, the dominant FFT frequency is 7.49 Hz and in the separation region is mostly 1.9 Hz both of which are obvious features of the EFD data without recourse to the CFD as with the wave elevations. Similarly, the URANS and DES dominant FFT frequency foil-surface pressure shows three distinct regions that correspond to the three different instability mechanisms: 2 Hz inside the separation bubble, 0.74 Hz outside the reattachment, and 0.32 Hz which envelopes the other two. All three are also evident in the EFD, but not quite as distinct.

Foil-surface pressure time histories with running mean and r.m.s., FFT, and PSD are closely examined for medium Fr to identify regions with steady and unsteady response and for the latter dominant, intermittent, or broad-banded FFT frequencies. Unsteady responses show a high dominant FFT frequency (7.49 Hz) in a small region near the bow with low r.m.s. values and a region of SL (1.9 Hz), Karman (0.86 Hz), and flapping (0.31 Hz) dominant FFT frequencies in a large region of high r.m.s. Both cases are bounded by regions of intermittent response. At greater depths the response is broad banded, which is likely due to model vibration. Responses labelled in Fig. 3 with time histories, expanded views of time histories, and FFT and PSD at representative locations are shown in Fig. 11. Fig. 11(a) shows high dominant FFT frequency response with relatively low r.m.s. oscillations evident, especially in the expanded view

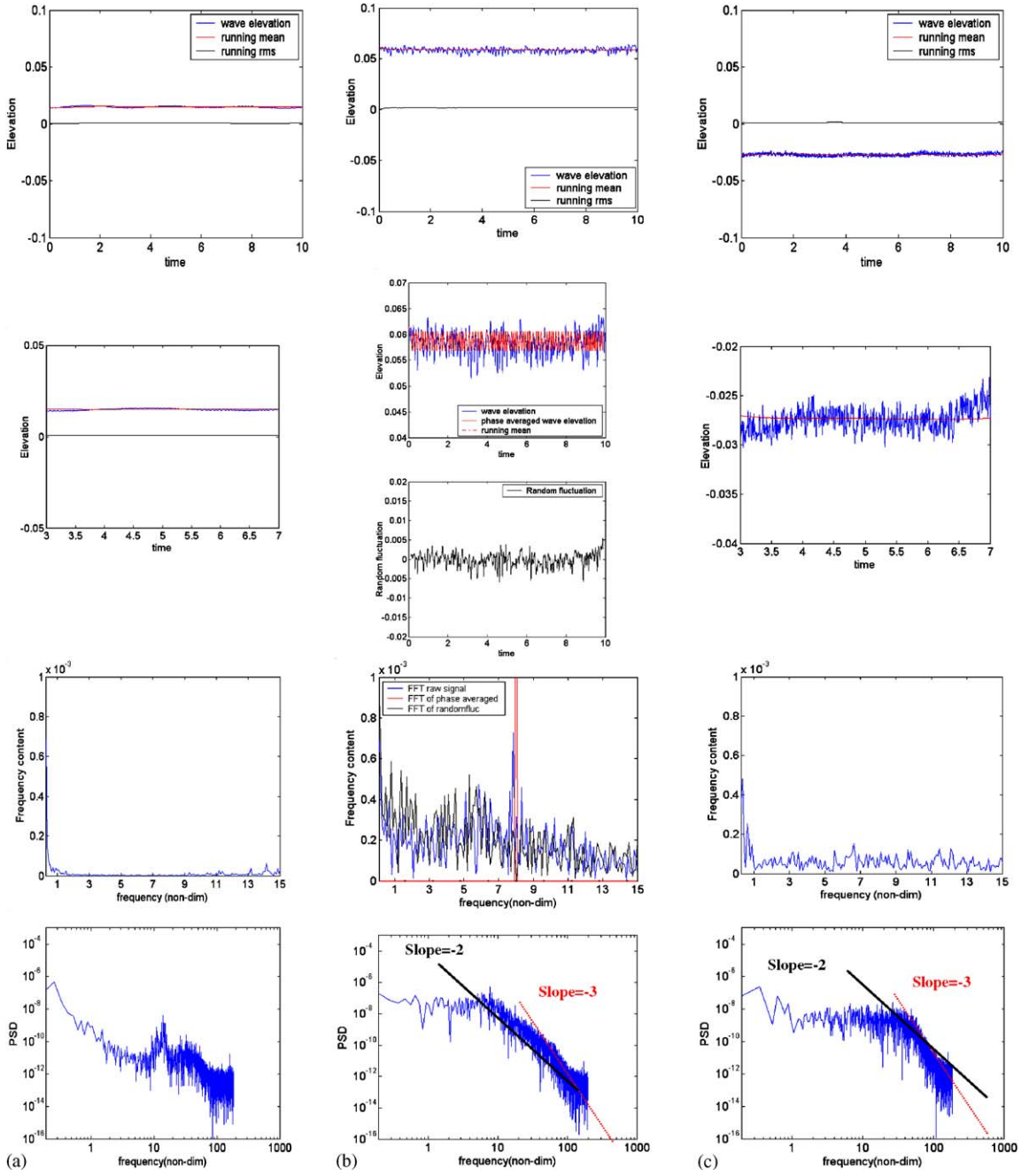

Fig. 7. Time histories, expanded views of phase-averaged time histories, FFT and power-spectral densities of free-surface wave elevation (Fr = 0.37): (a) $x = -0.28$, $y = 0.0$, steady flow; (b) $x = -0.0325$, $y = 0.015$, bow wave (FFT amplitude $\geqslant 0.0004$) Frequency = 8.33 Hz, Nondimensional frequency = 7.86, $T = 0.12$ s; (c) $x = 0.215$, $y = 0.258$; low amplitude intermittent; (d) $x = 0.49$, $y = 0.1275$ SL (FFT amplitude $\geqslant 0.002$) Frequency = 1.99 Hz, Nondimensional frequency = 1.89, $T = 0.5$ s; (e) $x = 0.8475$, $y = 0.1158$, Karman (FFT amplitude $\geqslant 0.002$) Frequency = 0.90 Hz, Nondimensional frequency = 0.85, $T = 1.11$ s; (f) $x = 0.9025$, $y = 0.3498$, flapping (FFT amplitude $\geqslant 0.002$) Frequency = 0.3 Hz, Nondimensional frequency = 0.284, $T = 3.3$ s; (g) $x = 0.71$, $y = 0.4102$, high amplitude intermittent and (h) $x = 1.425$, $y = 0.459$, broad banded.

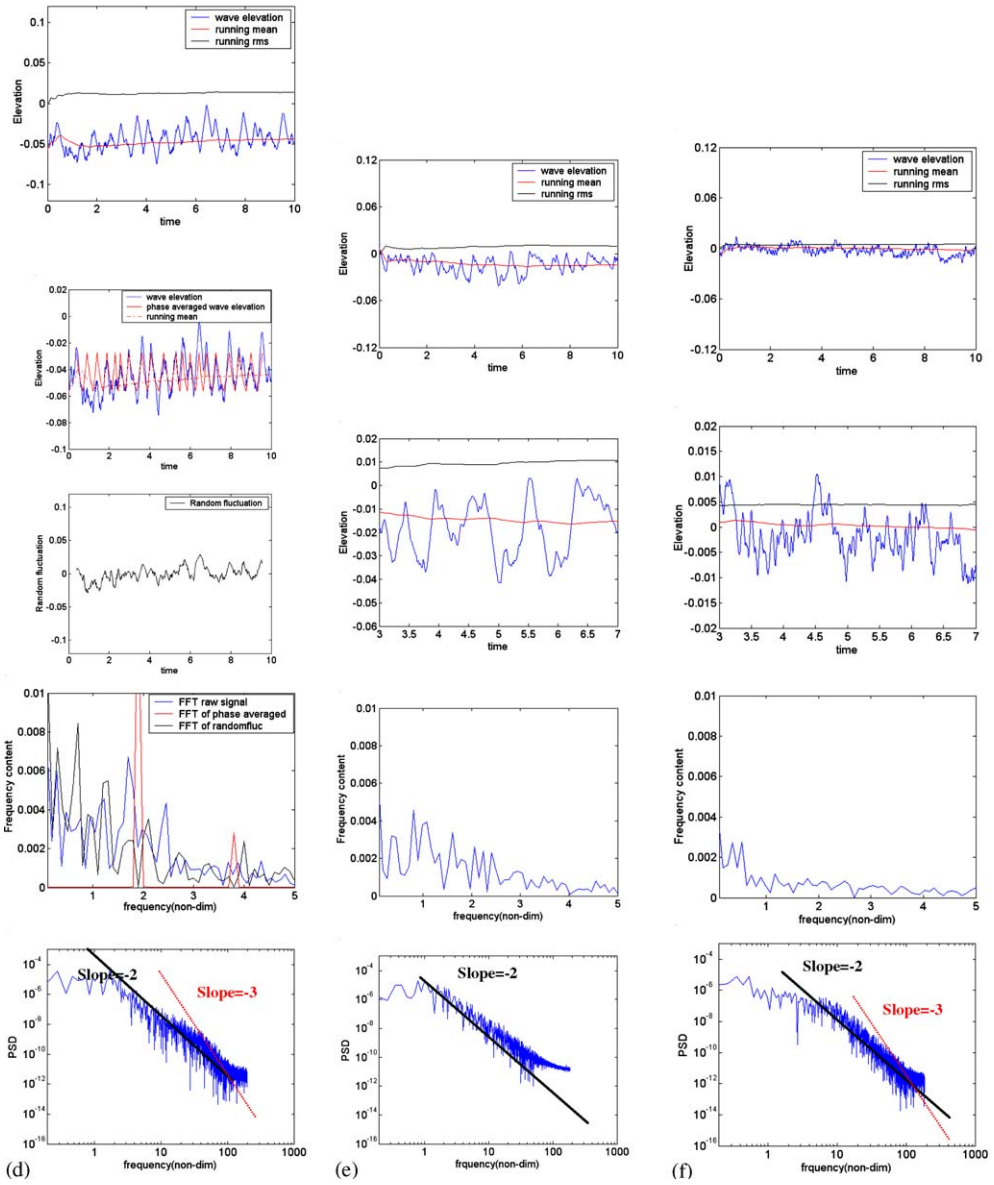

Fig. 7. (*Continued*)

and FFT. Fig. 11(b) shows SL dominant FFT frequency response with relatively large r.m.s. oscillations, especially in the expanded view and FFT. High and SL dominant FFT frequency responses clearly display effects of both organized and random fluctuations such that the r.m.s. includes both. In the former region, the time histories are insufficiently dominated by the organized oscillations to enable decomposition, whereas in the SL frequency region the organized and random component average values are evenly distributed at 15% of DR_{Cp} each, as also shown in Fig. 11(b) and Table 6. Organized oscillations display narrow-banded FFT, whereas random fluctuations display broad-banded FFT. Figs. 11(c) and (d) show Karman and flapping responses. Figs. 11(e) and (f) show intermittent and broad-banded responses with relatively low and very low r.m.s. oscillations and no peaks in the FFT. For all unsteady responses (except at the greater depths), PSD shows high-frequency dissipation with slopes of about $-\frac{5}{3}$, as expected for the decay of turbulence.

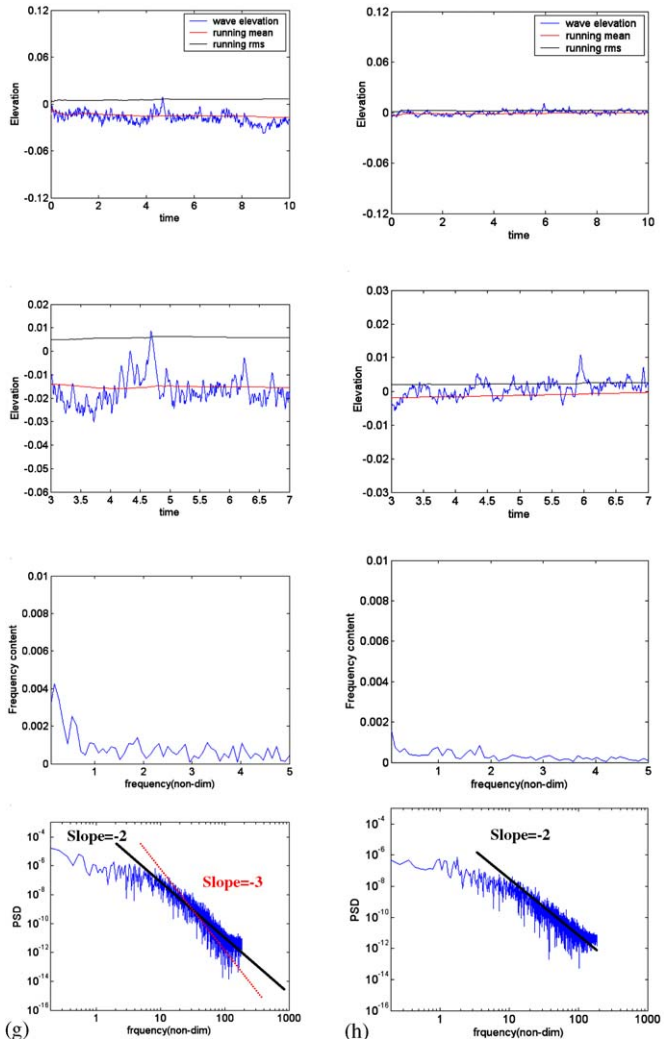

Fig. 7. (*Continued*)

4. Conclusions

Experiments of unsteady free-surface, wave-induced, boundary-layer separation are conducted in a $3.05 \times 3.05 \times 100\,m^3$ towing tank for a surface-piercing NACA 0024 foil, which has insignificant separation, nowave effects, and 2-D flow for the deep condition. Test conditions are selected for minimal, reattaching, and non-reattaching separation for $Fr = 0.19$, 0.37, and 0.55 and $Re = 0.822$, 1.52, and 2.26×10^6. For $Fr = 0.19$, no separation and the expected Kelvin waves are observed, whereas for medium and high Fr a wedge-shaped separation region is evident on the free surface. For $Fr = 0.37$, the separation region on the free and foil surfaces is demarcated by large r.m.s. (15–20% of the mean value dynamic range) and 1.94, 0.82, and 0.30 Hz dominant FFT frequency regions corresponding to shear layer, Karman, and flapping instabilities, respectively. A large bow wave resembles a spilling breaker with low r.m.s. (2–5% of the mean value dynamic range) and 8.5 Hz dominant FFT frequency on the free and foil-surfaces. Mean wave elevations in the separation region are relatively constant with intense free-surface oscillations, turbulence, and breaking. Outside the separation and wake region, the Kelvin waves are evident. The foil-surface pressure is high in the bow wave, low in the wave trough, with a gradual rise towards the trailing edge, and recovery of 2-D foil-surface pressure distributions for large depths. For $Fr = 0.55$, the bow wave is enormous. The separation region is shifted

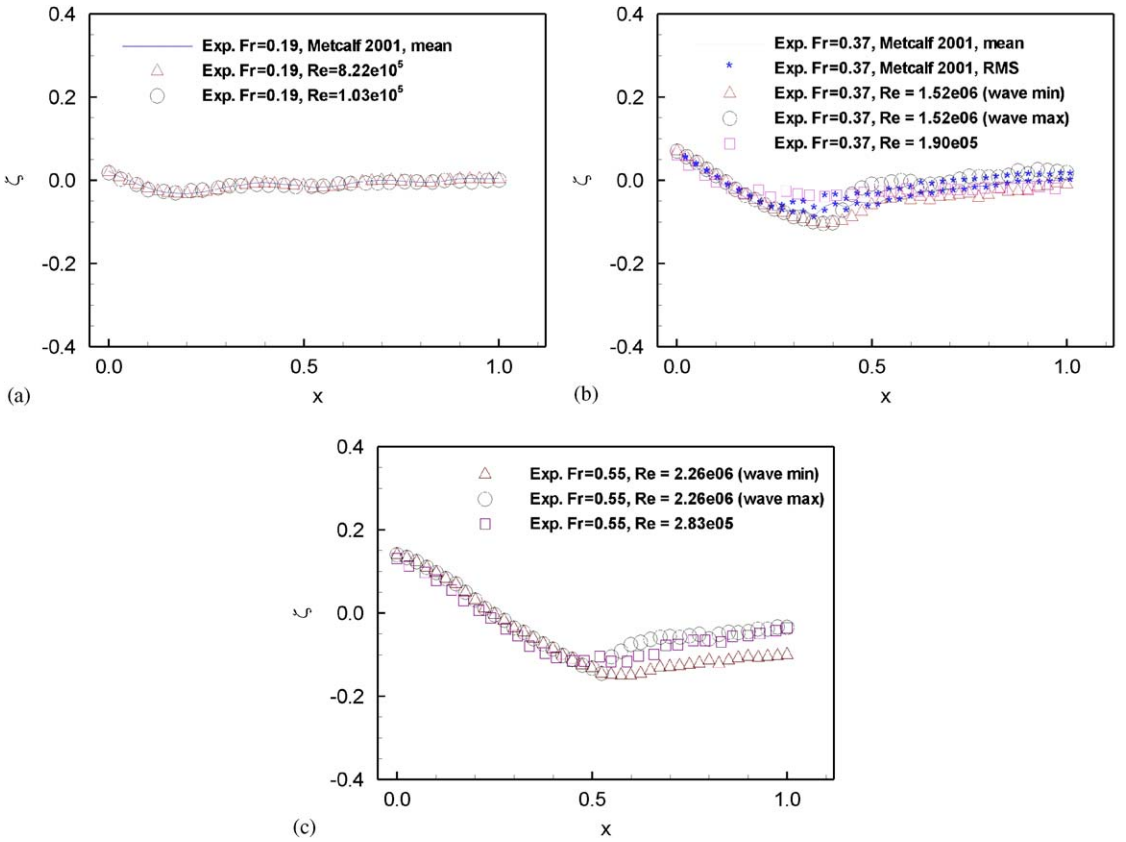

Fig. 8. Wave profiles and near-field elevations close to the foil surface: (a) Fr = 0.19; (b) Fr = 0.37 and (c) Fr = 0.55.

towards the trailing edge with increased splashing and bubbles. The Kelvin waves are no longer distinguishable due to increased free-surface turbulence. Mean foil-surface pressure, free-surface, and bottom effects interact.

The complexity of unsteady, wave-induced, boundary-layer separation makes detailed flow measurements difficult and usually results in only sparse data, however, when combined with CFD studies (Kandasamy et al., 2005; Xing et al., 2005) a credible description of the flow physics can in fact be provided. Normalized Strouhal numbers for shear layer instability (St_θ scaled by the momentum thickness at separation θ), Karman instability (St_h scaled by the half-wake thickness h), and flapping instability (St_R scaled by the mean reattachment length X_R) show the effects of free surface and Fr on the instability mechanisms. Instability studies include laminar cases too. Time evolution study of the vortical structures show their formation and shedding mechanisms, and their relation to already-known separation patterns. The turbulent case (Fr = 0.37) has reattaching separation with dominant shear layer shedding ($St_\theta = 0.0077$), and weaker Karman-like shedding ($St_h = 0.066$). The Fr = 0.55 case has nonreattaching separation with similar dominant shear layer shedding ($St_\theta = 0.0052$), and weaker Karman shedding ($St_h = 0.068$). The results support previous observations that the free surface reduces both the strength and frequency of large-scale vortex shedding. DES provides more resolved turbulence and anisotropy effects and analysis of Reynolds stress budgets and invariant maps. DES with free-surface tracking and level-set approaches do not show major topological differences compared to the URANS solutions providing confidence in the predicted flow topology downstream of separation. Solutions of DES with the level-set method show improved prediction of wave amplitudes (reduced) and separation bubble size (increased).

Future experiments should focus on unsteady wave elevation and foil-surface pressure measurements for high Fr and unsteady PIV, and void fraction measurements for both medium and high Fr. Physical understanding of unsteady, free-surface, wave-induced boundary-layer separation aids in the understanding of practical applications, as recently shown for ship maneuvering (Pinto-Heredero, 2005).

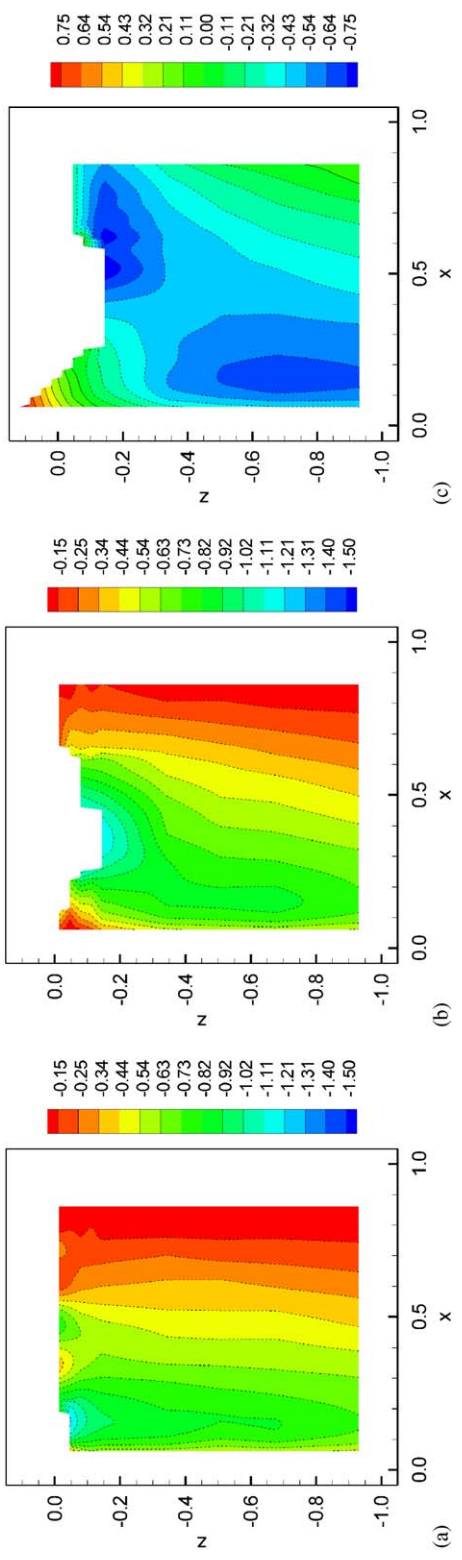

Fig. 9. Foil-surface pressure—mean: (a) Fr = 0.19; (b) Fr = 0.37 and (c) Fr = 0.55.

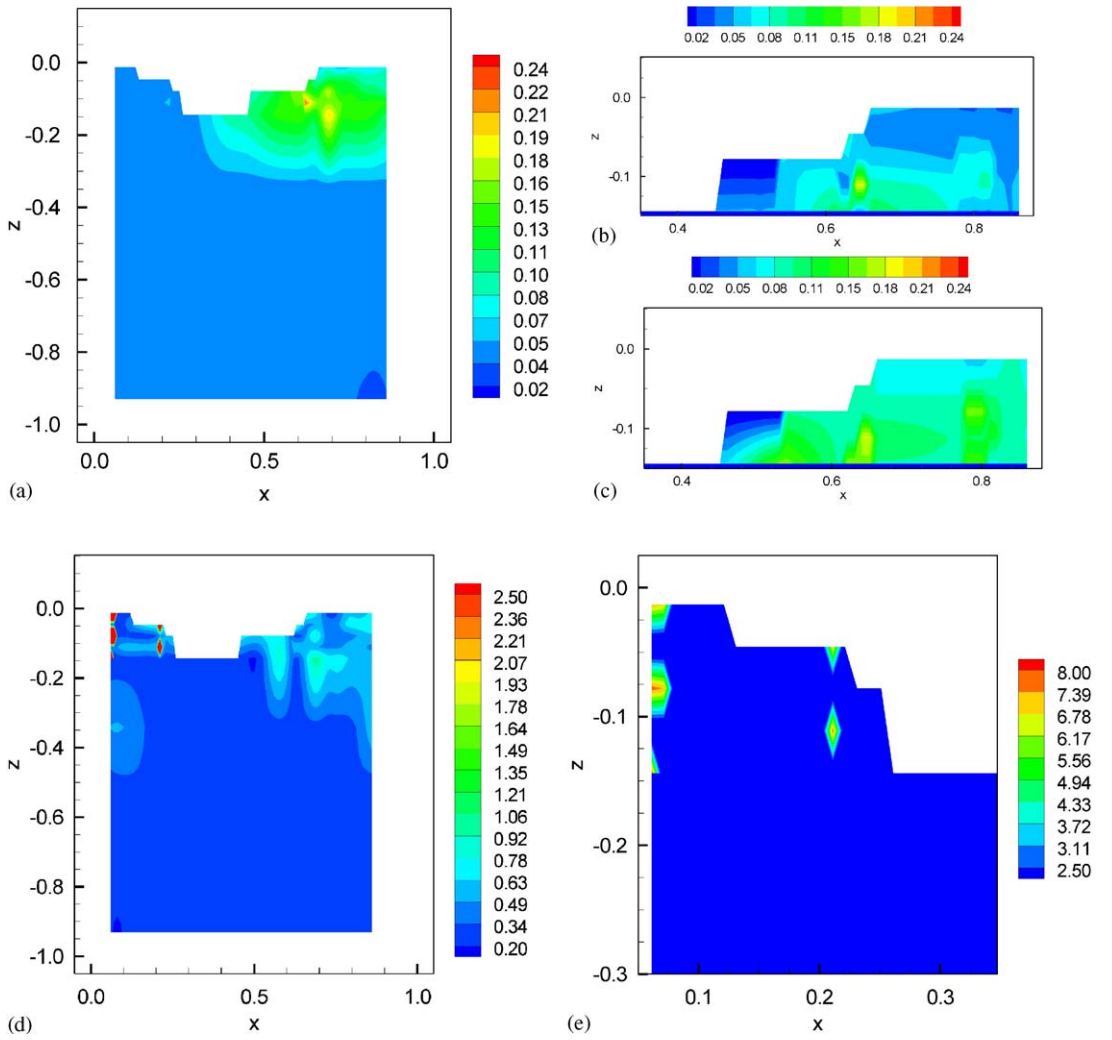

Fig. 10. Foil-surface pressure, r.m.s., and dominant frequency for Fr = 0.37: (a) r.m.s. of raw signal; (b) r.m.s. of organized oscillation (dominant frequency region); (c) r.m.s. of random fluctuation (dominant frequency region); (d) dominant FFT frequency and (e) expanded view of dominant FFT frequency region.

Table 6
R.m.s. of foil surface pressure for Fr = 0.37

	Surface pressure (Dynamic range, $DR_{Cp} = 1.183$)			
	Bow region	Separation region		
	Raw	Raw	Organized	Random
r.m.s. (average)	0.0442	0.121	0.06024	0.0905
r.m.s. (max)	0.0560	0.234	0.1822	0.1776
r.m.s. (max)/DR_{Cp}	4.73%	19.78%	15.40%	15.01%

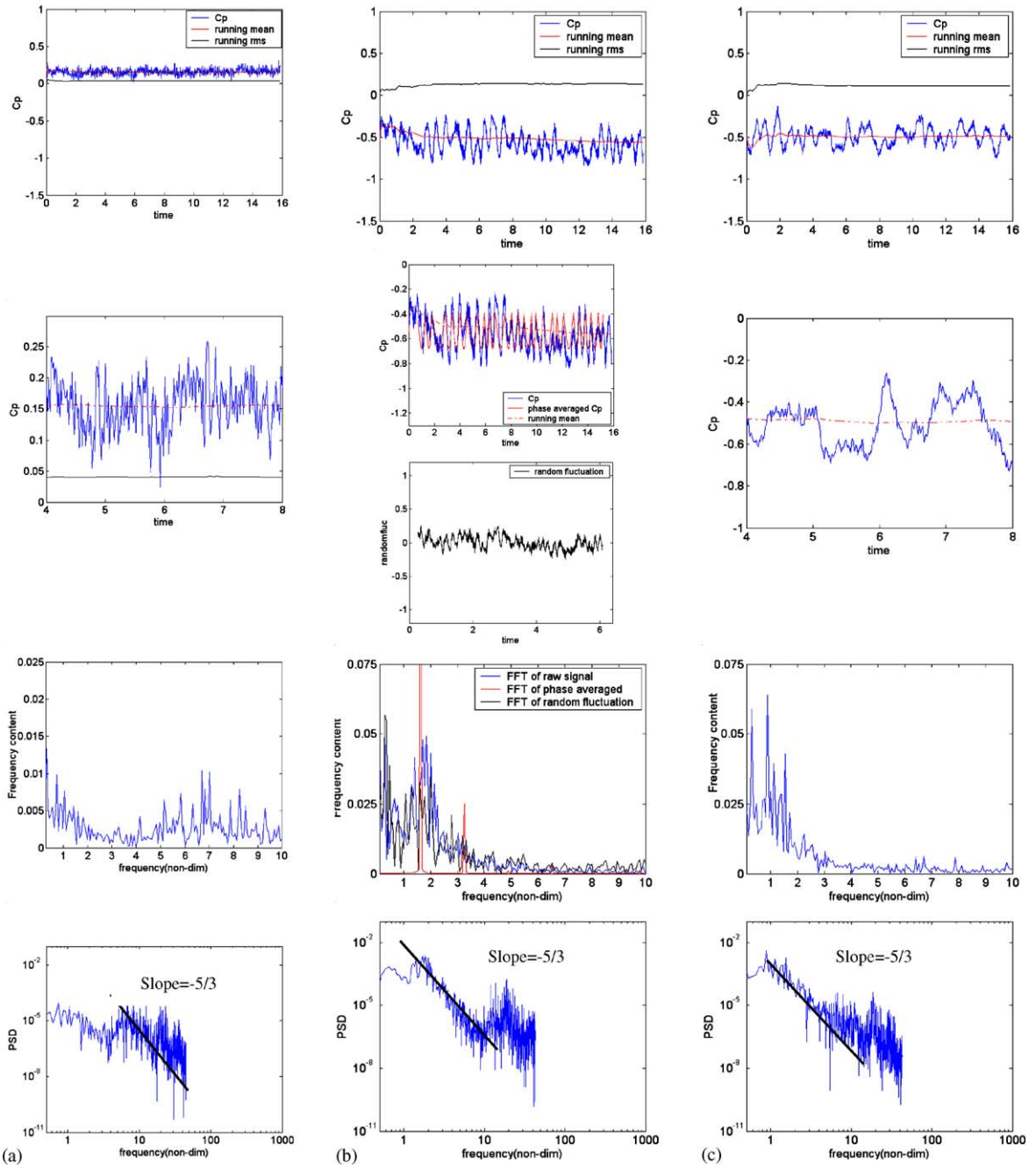

Fig. 11. Time histories, expanded views of phase-averaged time histories, FFT and power-spectral densities of surface pressure (Fr = 0.37): (a) $x = 0.0613$, $z = -0.0129$, bow wave (FFT amplitude $\geqslant 0.01$) Frequency = 7.69 Hz, Nondimensional frequency = 7.26, $T = 0.13$ s; (b) $x = 0.6478$, $z = -0.0459$, SL (FFT amplitude $\geqslant 0.02$) Frequency = 1.94 Hz, Nondimensional frequency = 1.84, $T = 0.52$ s; (c) $x = 0.6478$, $z = -0.0780$, Karman (FFT amplitude $\geqslant 0.02$) Frequency = 0.99 Hz, Nondimensional frequency = 0.94, $T = 1$ s; (d) $x = 0.836$, $z = -0.1437$, flapping (FFT amplitude $\geqslant 0.02$), Frequency = 0.296 Hz, Nondimensional frequency = 0.28, $T = 3.38$ s; (e) $x = 0.5413$, $z = -0.3415$, intermittent and (f) $x = 0.2213$, $z = -0.5075$, broad banded.

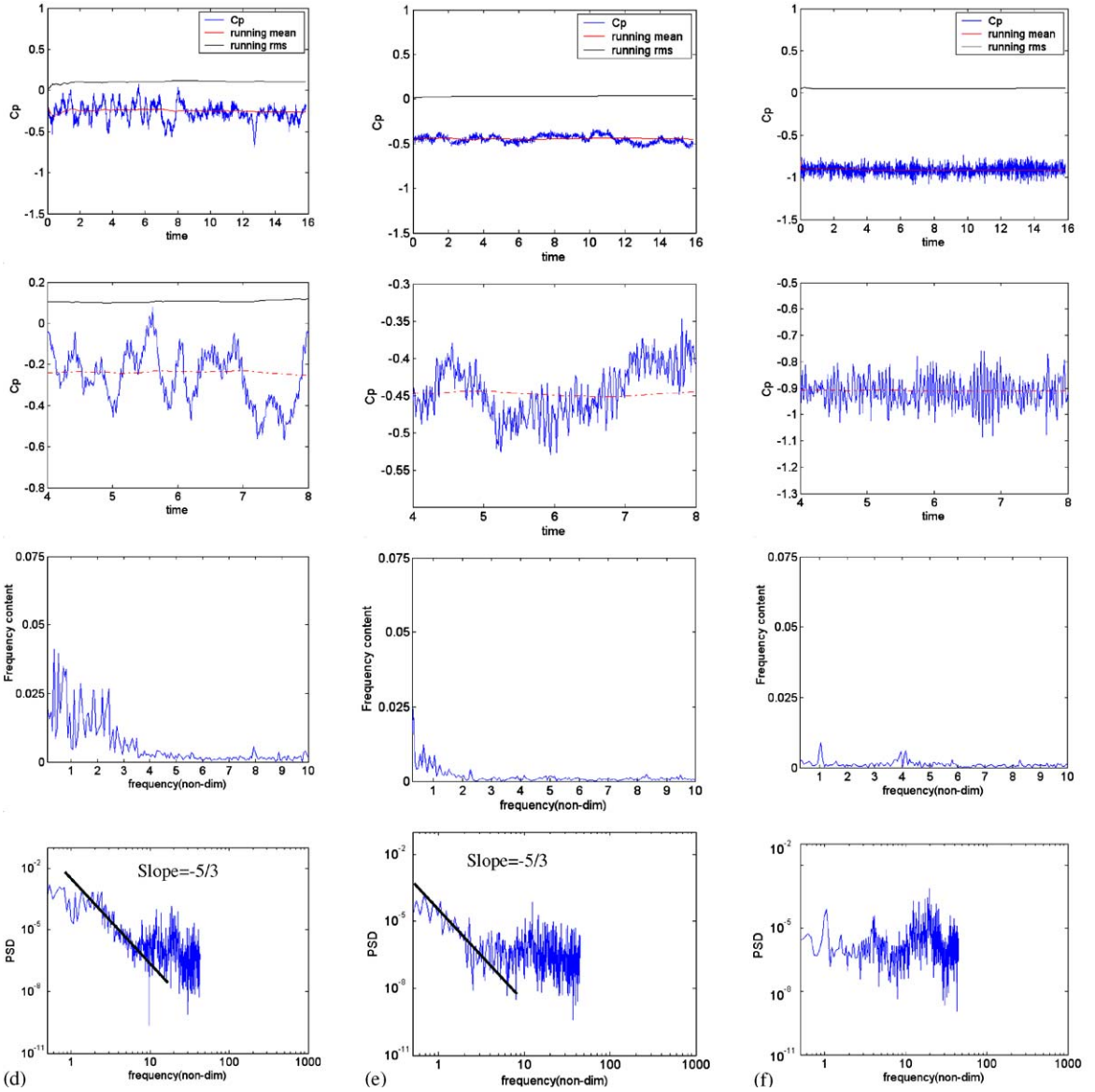

Fig. 11. (*Continued*)

Acknowledgements

This research is sponsored by the Office of Naval Research under Grant N00014-01-1-0073, under the administration of Dr Patrick Purtell.

References

ASME, 1998. Test Uncertainty. ASME PTC 19.1-1998. The American Society of Mechanical Engineers.

Chen, T., Chwang, A.T., 2002. Trailing vortices in a free-surface flow. Physics of Fluids 14, 827–838.

Chow, S.K., 1967. Free-surface effects on boundary layer separation on vertical struts. Ph.D. Thesis, The University of Iowa, Iowa City, IA.

Eisele, K., Öngören, A., Holbein, P., Casey, M.V., Ursenbacher, T., Monkewitz, P.A., 2000. Benchmark for measurements in a planar diffuser with a high inlet turbulence level. In: Proceedings of the 10th International Symposium on Applications of Laser Techniques to Fluid Mechanics, Session 14, 14.6, Lisbon, Portugal.

ITTC, 2002. Quality Manual, 23rd International Towing Tank Conference. Venice, Italy.

Kandasamy, M., 2001. RANS simulation of free-surface wave induced separation around a surface piercing NACA-0024 hydrofoil. M.S. Thesis, Department of Mechanical Engineering, The University of Iowa, Iowa City, IA.

Kandasamy, M., Xing, T., Stern, F., 2005. Unsteady free-surface wave induced separation: coherent vortical structures and instabilities, Journal of Fluids and Structures, submitted for publication (also Kandasamy, M., 2005. Ph.D. Thesis, Department of Mechanical Engineering, The University of Iowa, Iowa City, IA).

Kawamura, T., Mayer, S., Garapon, A., Sorensen, L., 2002. Large eddy simulation of a flow past a free surface piercing circular cylinder. Journal of Fluids Engineering 124, 91–101.

Kiya, M., Mochizuki, O., Ishikawa, H., 2000. Challenging issues in separated and complex turbulent flows. In: Proceedings of the 10th International Symposium on Applications of Laser Techniques to Fluid Mechanics, Session 19, 19.0, Lisbon, Portugal.

Li, C., Lin, P., 2001. A numerical study of three-dimensional wave interaction with a square cylinder. Ocean Engineering 28, 1545–1555.

Lin, P., Li, C.W., 2003. Wave–current interaction with a vertical square cylinder. Ocean Engineering 30, 855–876.

Longo, J., Stern, F., 2005. Uncertainty assessment for towing tank tests with example for surface combatant DTMB model 5415. Journal of Ship Research 49, 55–68.

Metcalf, B., 2001. Rans experimental investigations on free-surface wave induced separation. M.S. Thesis, Department of Mechanical Engineering, The University of Iowa, Iowa City, IA.

Orlins, J.J., Gulliver, J.S., 2000. Measurements of free surface turbulence. In: Proceedings of the Fourth International Symposium on Gas Transfer at Water Surfaces. Miami Beach, Florida.

Oshkai, P., Rockwell, D., 1999. Free surface wave interaction with a horizontal cylinder. Journal of Fluids and Structures 13, 935–954.

Pinto-Heredero, A., 2005. URANS and DES for Wigley hull at extreme drift angles. M.S. Thesis, Department of Mechanical Engineering, The University of Iowa, Iowa City, IA.

Pogozelski, E.M., Katz, J., Huang, T.T., 1997. Flow structure around a surface piercing strut. Physics of Fluids 9, 1387–1399.

Sheridan, J., Lin, J.-C., Rockwell, D., 1997. Flow past a cylinder close to a free surface. Journal of Engineering and Applied Science 330, 1–30.

Simpson, R.L., 2001. Junction Flows. Annual Review of Fluid Mechanics 33, 415–443.

Stern, F., Hwang, W.S., Jaw, S.Y., 1989. Effects of waves on the boundary layer of a surface-piercing flat plate: experiment and theory. Journal of Ship Research 33, 63–80.

Stern, F., Choi, J.E., Hwang, W.S., 1993. Effects of waves on the wake of a surface-piercing flat plate: experiment and theory. Journal of Ship Research 37, 102–118.

Stern, F., Olivieri, A., Shao, J., Longo, J., Ratcliffe, T., 2005. Statistical approach for estimating intervals of certification or biases of facilities or measurement systems including uncertainties. ASME Journal of Fluids Engineering 127, 604–610.

Sung, J., Yoo, J.Y., 2001. Three dimensional phase averaging of time-resolved PIV measurement data. Measurement Science Technology 12, 655–662.

Xing, T., Kandasamy, M., Stern, F., 2005. Unsteady free-surface wave induced separation: turbulent structures, in preparation (also Xing, T., Kandasamy, M., Wilson, R. Stern, F., 2004. DES and RANS of Unsteady Free-surface Flows. In: Proceedings of the 42nd AIAA Aerospace Sciences Meeting, Reno, Nevada, Division for Fluid Dynamics).

Zhang, Z.J., Stern, F., 1996. Free-surface wave-induced separation. ASME Journal of Fluids Engineering 118, 546–554.